Reprinted from

CMES

Computer Modeling in Engineering & Sciences

Founder and Editor-in-Chief:
Satya N. Atluri

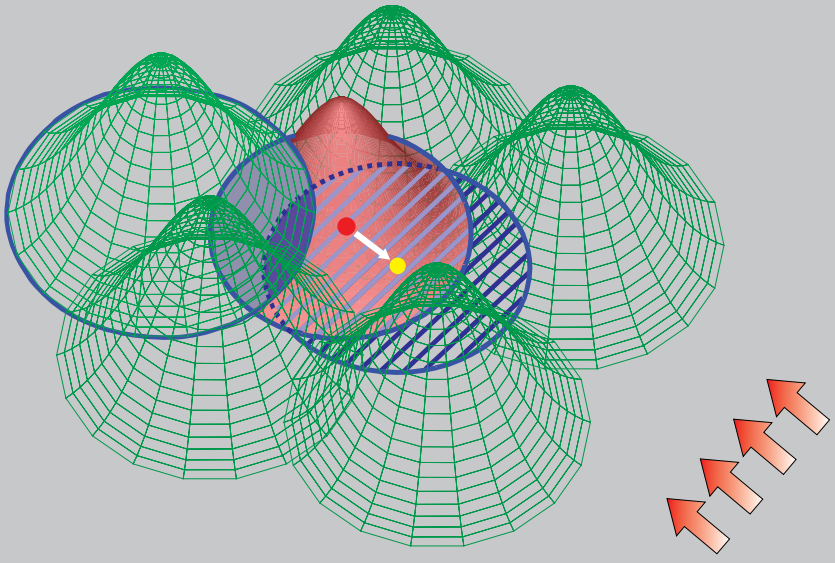

ISSN: 1526-1492 (print)
ISSN: 1526-1506 (on-line)

Tech Science Press

 CMES, vol.83, no.3, pp.221-248, 2012

An Adaptive Extended Kalman Filter Incorporating State Model Uncertainty for Localizing a High Heat Flux Spot Source Using an Ultrasonic Sensor Array

M.R. Myers[1], A.B. Jorge[2], D.E. Yuhas[3] and D.G. Walker[1]

Abstract: An adaptive extended Kalman filter is developed and investigated for a transient heat transfer problem in which a high heat flux spot source is applied on one side of a thin plate and ultrasonic pulse time of flight is measured between spatially separated transducers on the opposite side of the plate. The novel approach is based on the uncertainty in the state model covariance and leverages trends in the extended Kalman filter covariance to drive changes to the state model covariance during convergence. This work is an integral part of an effort to develop a system capable of locating the boundary layer transition region on a hypersonic vehicle aeroshell. Results from thermal conduction experiments involving one-way ultrasonic pulse time of flight measurements are presented. Comparisons between the adaptive extended Kalman filter and a non-adaptive extended Kalman filter are presented. Heating source localization results and convergence behavior are compared for the two filters. This work provides evidence that, for the subject heating source localization problem, the state model covariance and measurement covariance in the extended Kalman filter are correlated in an inversely proportional manner. Modifications to either the state model covariance or the measurement covariance effects the convergence behavior of the Kalman filter. The extended Kalman filter variance was observed to increase until convergence and to decrease rapidly after convergence. The variance was used to drive modifications to the state model covariance in a manner designed to affect convergence behavior. The adaptive extended Kalman filter developed in this work produces faster and smoother convergence than the non-adaptive form of the extended Kalman filter. This performance boost is accomplished by tailoring the state model covariance during each iteration instead of retaining the assumed state model covariance throughout the convergence process.

[1] Vanderbilt University, Nashville, TN, USA.
[2] Federal University of Itajubá, Itajubá, MG, Brazil.
[3] Industrial Measurement Systems, Inc., Aurora, IL, USA.

Keywords: ultrasonic thermometry, ultrasound, localization, adaptive extended Kalman filter

1 Nomenclature

A	area (m^2); amplitude (m); state Jacobian
a	state model; material thickness
B	measurement Jacobian
b	expected measurement
C	heat capacity (J/K)
c_p	specific heat (J/kg K)
c	distance from ellipse center to ellipse edge along the major axis
d	distance from ellipse center to ellipse edge along the minor axis
E	energy (J); Young's modulus (GPa)
F	cumulative density function
G	ultrasonic time of flight (s)
$\overline{G}$	expected ultrasonic time of flight (s)
h	convection heat transfer coefficient (W/m^2-K)
I_n	$n \times n$ identity matrix
K	Kalman gain
k	thermal conductivity ($W/m-K$)
M	adaptive extended Kalman filter gain
Q	heat source; state model covariance
q''	heat flux (W/m^2)
R	thermal resistance (K/W); measurement covariance
S	sensitivity
T	temperature (K)
t	time (s)
U	control input
v	sound speed (m/s)

w	width (m);
X	state
$\overline{X}$	predicted state
x, y, z	rectangular coordinates (m)
$\overline{x}, \overline{y}$	predicted rectangular coordinates (m)
Z	actual measurements

Greek letters

Δ	normalized temperature difference
∇	Laplacian operator
δ	coefficient
θ	temperature change relative to reference (K)
$\overline{\theta}$	predicted temperature change relative to reference (K)
ξ	ultrasonic time of flight temperature factor (1/K)
ρ	density (kg/m^3)
Σ	state covariance
$\overline{\Sigma}$	predicted covariance
σ^2	variance for a Gaussian probability density function

Subscripts

0	initial or zero point
amb	ambient
i	sensor
inf	infinity
j	sensor
g	Gaussian profile
q	heat source
s	heat source
T	temperature
t	time (s)
ts	time-scaling coefficient

2 Introduction

An ultrasonic sensor, extended Kalman filter solution has been explored in previous work to locate concentrated heating sources [Myers, Jorge, Mutton, and Walker (2012b,a)]. This work extends the previous research by developing an adaptive extended Kalman filter to obtain faster and smoother convergence. The push for convergence performance becomes paramount when moving sources are considered.

The measurement covariance, utilized by the extended Kalman filter, can be obtained from sensor noise analysis. The state model covariance, however, is entirely unknown and is obtained through trial and error. A state model covariance with values in a certain range results in smooth filter convergence while a state model covariance with values outside of a certain range results in erratic convergence or convergence failure. This work examines the possibility that the state model covariance and the measurement covariance are correlated and if they are correlated, is there a way to tailor the state model covariance for each extended Kalman filter iteration.

The adaptive extended Kalman filter developed in this work is unique when compared to adaptive extended Kalman filters found in the existing literature. In the 1960s, the effect of erroneous models on the Kalman filter response was explored [Heffes (1966)] and adaptive Kalman filtering with unknown state and measurement covariance matrices was investigated [Mehra (1969)]. More recently, the extended Kalman filter was combined with recursive least squares to solve inverse heat conduction problems [Tuan and Ju (2000); Wang, Chen, Tuan, and Den (2005)]. Adaptive extended Kalman filters have been described for structural damage detection [Yang, Lin, Huang, and Zhou (2006); Zhou, Wu, and Yang (2008)] and adaptive control [Yucelen and Calise (2010)]. Additionally, models with correlated parameters have been analyzed [Xu and Gertner (2008)].

This work is applicable to numerous industries including manufacturing and aerospace. Primary motivation for this work comes from the aerospace industry in that knowledge of where air flowing across a body transitions from laminar flow to turbulent flow can provide numerous benefits to air vehicle design, thermal protection system design, and air vehicle in-flight control [Reed, Kimmel, Schneider, Arnal, and Saric (1997)]. Directly observing and measuring the transition region in an operational vehicle is difficult because the harsh environment presents numerous challenges including high-speed airflow and high surface temperatures [Fay and Riddell (1958); Kendall (1975); Schook, Lange, and Steenhoven (2001); Gai and Hayne (2010)]. The novel measurement system proposed in this and previous work leverages the hypersonic body-surface heating profile documented in the literature [Horvath, Berry, and Hollis (2002); Schneider (1999, 2004); Berger, Rufer, Kimmel, and Adamczak (2009)] to locate the boundary layer transition region. The sensors would be located on the inside surface of the aeroshell away from the harsh external conditions. Consequently, the phenomenon that is being measured is not disturbed and the sensor is not exposed to the harsh environment present at the aeroshell surface. The solution investigated in this work involves a forward conduction solution and an inverse procedure based on the extended Kalman filter. Kalman filters construct a framework of predicting the state based on an input to

the system and correcting the predicted state based on sensor observations [Majji, Juang, and Junkins (2010); Bertsekas (1996)]. Kalman filters were invented by Peter Swerling (1958) and Rudolf Kálmán (1960) as a technique for filtering and prediction in linear Gaussian systems [Thrun, Burgard, and Fox (2006)]. Kalman filters have proven popular in guidance and navigation systems [Thrun, Burgard, and Fox (2006)] and other state estimation and inverse scenarios [Rochinha and Peirce (2010); Maier, Bocciarelli, Bolzon, and Fedele (2006); Corigliano, Mariani, and Orsatti (2000); Corigliano and Mariani (2004); Gan and Danai (2001)]. Kalman filters, however, have not seen much activity in heat transfer applications [Vianna, Orlande, and Dulikravich (2009); Park and Jung (2001)].

Simple, controlled experiments involving concentrated high heat flux sources on a large flat metal plate are used to develop the proposed measurement method. Both high heat flux spot sources and high heat flux step sources are considered; however, the work presented here is restricted to the high heat flux spot source. Previous work details a thermocouple experiment with a high heat flux spot source [Myers, Jorge, Walker, and Mutton (2010b); Myers, Jorge, Mutton, and Walker (in press, 2012)], a forward conduction solution [Myers, Jorge, Walker, and Mutton (2010b); Myers, Jorge, Mutton, and Walker (in press, 2012)], six different measurement models for the inverse procedure [Myers, Jorge, Walker, and Mutton (2010a); Myers, Jorge, Mutton, and Walker (in press, 2012)], a sensor array and sensitivity to boundary conditions, thermal properties, and noise [Myers, Jorge, Mutton, and Walker (2012b)], and a comparison of extended Kalman filter, particle filter, and least squares localization techniques [Myers, Jorge, Mutton, and Walker (2012a)]. The particle filter is an alternative nonparametric implementation of the Bayes filter and is a Monte Carlo technique used for the solution of state estimation problems. Ordinary least squares is applied to approximate solutions of overdetermined systems, i.e. systems of equations in which there are more equations than unknowns. Ordinary least squares is often applied in statistical contexts, particularly regression analysis. Other probabilistic computer methods such as genetic algorithms [Raudenský, Woodbury, Kral, and Brezina (1995)], polynomial chaos [Ghanem and Spanos (1990)], and stochastic perturbation methods [Kamiński (2005)] have not been considered. Primary conclusions from previous work considering a high heat flux spot source are: 1) least squares, extended Kalman filter, information filter, and particle filter produce similar results, 2) measuring one-way ultrasonic time-of-flight produces better localization results than measuring ultrasonic pulse-echo time of flight, and 3) sensitivity to heating source location is greater in the direction perpendicular to the ultrasonic pulse propagation path.

Table 1: Material properties for the stainless steel 316L test sample used in the conduction experiments.

Property	Value
density (ρ)	$8,000\,\mathrm{kg/m^3}$
thermal conductivity (k)	$14.6\,\mathrm{W/mK}$
specific heat (c_p)	$500\,\mathrm{J/kgK}$
sound speed (v_0)	$5,100\,\mathrm{m/s}$ @ 293 K
ultrasonic TOF temperature factor (ξ)	$110\times10^{-6}\,1/\mathrm{K}$
sample length	61 cm
sample width	30.5 cm
sample height	0.635 cm

3 Flat Plate Experiment

This experiment was described and analyzed for a different problem in previous work [Myers, Jorge, Mutton, and Walker (2012a)] and is repeated here for the reader's convenience. This work concentrates first on a large flat plate heated over a small area with a known heat source. Consider a 6 cm x 30.5 cm x 0.635 cm stainless steel 316L plate (Figure 1) with constant properties (Table 1). The plate is large enough so the plate edges do not affect the temperature profile in the plate during the experiment. The heating source, a Research, Inc. SpotIR 4150 heater with focusing cone, is positioned approximately 2 mm from the plate surface such that its beam strikes a fixed position on the plate and is applied at $t = 300$ s and removed at $t = 600$ s. A parameter estimation study concluded the SpotIR heater has a heating profile of $q'' = 0.930\,\mathrm{MW/m^2}$ over 0.635 cm diameter circular area with a secondary heating modeled as a Gaussian with a profile of $q''_g = 100\,\mathrm{W/m^2}$ and a variance of $\sigma_g^2 = 0.0009\,\mathrm{m^2}$ (Figure 2) [Myers, Jorge, Walker, and Mutton (2010b); Myers, Jorge, Mutton, and Walker (in press, 2012, 2012b)]. The study also concluded the convection coefficient on the plate sides is $h = 3.20\,\mathrm{W/m^2\,K}$. The convection coefficient on the plate edges is assumed to be $h = 3\,\mathrm{W/m^2K}$ and radiation exchange between the plate and surroundings is assumed to be negligible.

Two ultrasonic sensors consisting of 2 MHz direct deposit transducers using Ferroperm Piezoceramics Pz46 are attached to the non-heated side of the plate. The direct deposit transducers are 1 cm diameter and 1 mm thick. With plate center on the heated side being the origin and the x-axis being the length (Figure 1), transducers are attached at ($x = -4$ cm, $y = 0$ cm) and ($x = 4$ cm, $y = 0$ cm) locations on the non-heated side ($z = 0.635$ cm). One transducer transmits ultrasonic pulses while

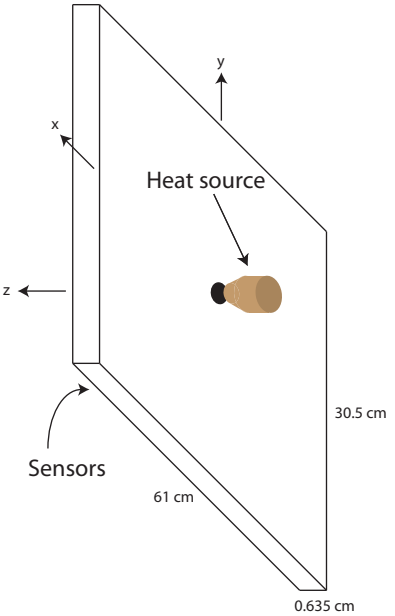

Figure 1: Illustration of flat plate with heat source and sensors (not drawn to scale) [Myers, Jorge, Mutton, and Walker (2012a)].

the other transducer receives the pulses, and time of flight is recorded. Separate experiments are conducted with the source positioned on the heated side of the plate at (x,y) locations of (0 cm, 0 cm), (0 cm, 2 cm), (0 cm, 4 cm), (0 cm, 6 cm), (0 cm, 8 cm), and (0 cm, 10 cm). Black Zynolyte® Hi-Temp Paint is applied to a 1.5 cm wide strip at the plate center to maximize energy absorption from the heater. The plate is oriented vertically with the positive y-axis pointing up. Data acquisition equipment employing cross-correlation techniques is used to determine and record ultrasonic pulse time of flight readings once per second during the experiment.

4 Forward Conduction Solution

The forward conduction solution used in this study was developed in previous work [Myers, Jorge, Walker, and Mutton (2010b,a); Myers, Jorge, Mutton, and Walker (in press, 2012, 2012b,a)] and is repeated here for the reader's convenience. The solution leverages COMSOL Multiphysics® by the COMSOL Group and MATLAB® by The Mathworks, Inc. The solution uses a finite element mesh with smaller elements near the heat source and larger elements near the plate edges to conserve computing resources.

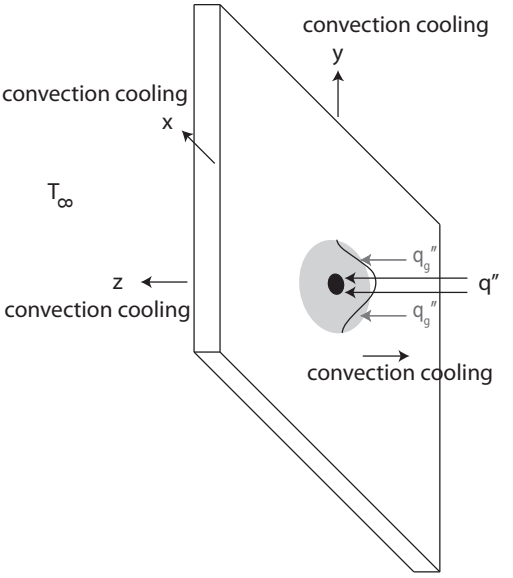

Figure 2: Illustration of boundary conditions on the flat plate [Myers, Jorge, Mutton, and Walker (2012a)] .

For the flat plate detailed in Section 3, the governing equation for the subdomain (conduction in the plate) is

$$\delta_{ts}\rho C_p \frac{\partial T}{\partial t} - \nabla \cdot (k\nabla T) = Q \tag{1}$$

where δ_{ts} is a time-scaling coefficient (1 in this case), ∇ is the Laplacian, and Q is an internal heat source (0 in this case). For the flat plate, k is assumed constant. Thus, the governing equation is

$$\nabla^2 T = \frac{\rho C_p}{k}\frac{\partial T}{\partial t} \tag{2}$$

where ∇ is the Laplacian and density (ρ), specific heat (C_p), and thermal conductivity (k) are considered constant.

The boundary condition is

$$n \cdot (k\nabla T) = q_0 + h(T_{inf} - T) \tag{3}$$

where n is the surface normal vector, q_0 is the inward heat flux and h is the convection coefficient. The convection coefficient (h) effectively includes convection and radiation cooling effects. The initial condition is an isothermal plate at $T = 297.5\,\mathrm{K}$.

A grid convergence study was performed to ensure grid independence [Roache (1998)]. Both the number of elements in the plate's $x-y$ plane and the number of layers in the plate's thickness were considered. An extruded mesh was generated by first creating 2D triangle elements in the plate's $x-y$ plane and then extruding the 2D mesh in the z-direction to create prism elements. Two subdomains consisting of a 0.635 cm diameter circle with a maximum element size of 1×10^{-3} m and a 6 cm diameter circle with a maximum element size of 5×10^{-3} m were used. The 2D mesh was created with the predefined normal free mesh setting in COMSOL®. The mesh extrusion process incorporates an option to create multiple mesh layers, therefore grid independence is contingent upon the number of layers through the thickness of the plate. The worst case is where the highest temperature gradients through the plate's thickness exist which is located at plate center. The grid convergence study led to the selection of three mesh layers through the plate's thickness dimension, 9,780 total elements, and 45,983 degrees of freedom. Independent verification of the COMSOL® solution was performed using a closed-form, analytical solution of heating through a circular domain without convection [Kozlov, Adamchik, and Lipovtsev (1989)]. Agreement between the COMSOL solution and the closed-form solution is acceptable with mean absolute error less than 0.5 K. The maximum temperature rise is approximately 80 K.

The measured time of flight is related to the average temperature between the transducers by [Myers, Walker, Yuhas, and Mutton (2008, in review, 2010)]

$$G_{ij} = \frac{R_{ij}}{v_0}\left(1+\xi\,\theta_{avg}|_i^j\right) \tag{4}$$

where R_{ij} is the distance between transducers (m), v_0 is the sound speed in the material at a reference temperature, ξ is the ultrasonic time of flight factor, which is material dependent (Table 1), and θ_{avg} is the change in temperature from the reference temperature between the two sensors. Since R_{ij} is known with insufficient accuracy to compare the time of flight from the model to the measured values, the time of flight can be normalized to the initial state eliminating the need to know R_{ij} and v_0 precisely.

$$\frac{G_{ij}}{G_0} = 1+\xi\left(T_{avg}|_i^j - T_0\right) \tag{5}$$

where G_0 is the average time of flight recorded at 1 s intervals from $t=1$ to 299 s before the heater is turned on. Figures 3 and 4 illustrate the agreement between the COMSOL® model and the ultrasonic time of flight measured during the experiment. The residuals [Beck and Woodbury (1998); Dowding and Blackwell (2001)] provide valuable insight into the accuracy of the model and indicate that the solution is somewhat biased. Agreement between the model and the experiment

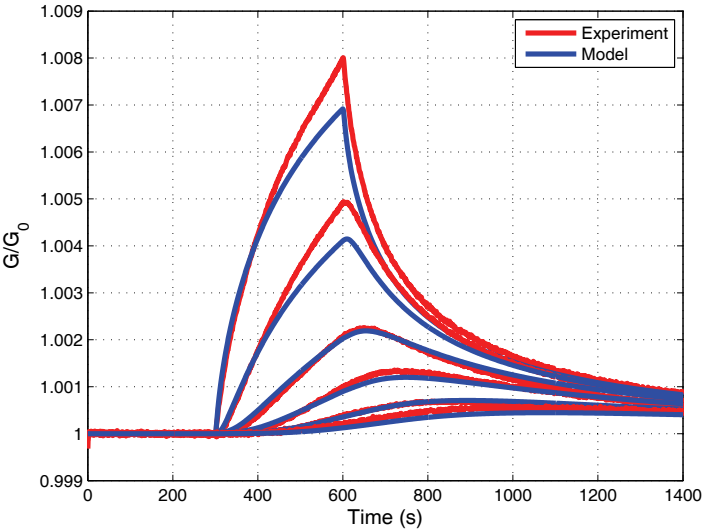

Figure 3: Comparison of the COMSOL® model with the one-way ultrasonic pulse experiment with heat source located between the sensors (top curve) and offset by 2 cm, 4 cm, 6 cm, 8 cmm, and 10 cm. The model uses temperatures along the non-heated surface of the plate [Myers, Jorge, Mutton, and Walker (2012a)].

is acceptable; however, the magnitude with the heat source located at ($x = 0$ cm, $y = 0$ cm) and when the heat source is located at ($x = 0$ cm, $y = 2$ cm) are both underestimated by the model. This difference is likely due to assumptions made about the size and profile of the heat source. Figure 5 illustrates the time of flight measurements during the beginning part of the experiment and highlights the time needed for the heat to reach the sensors.

5 Measurement Model

The measurement model examined in this work is based on a sensor array using four ultrasonic transducers in an 8 cm square pattern (Figure 6).

Locating and characterizing a heating source depends upon many factors such as heating source movements in time, heating source magnitude changes in time, and other transient behaviors (e.g., transient boundary conditions). Fairly restrictive assumptions can be imposed that simplify the problem. Analysis and algorithm development can proceed using these restrictive assumptions and then assumptions

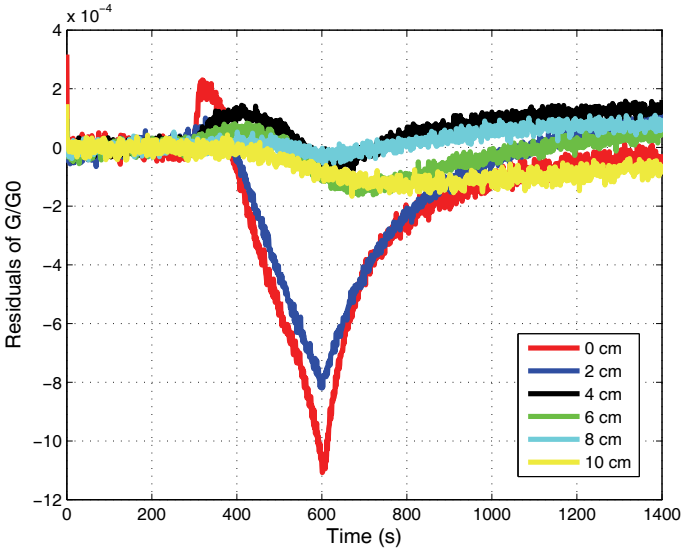

Figure 4: Residuals between the COMSOL® model and the one-way ultrasonic pulse experiment. The model uses temperatures along the non-heated surface of the plate [Myers, Jorge, Mutton, and Walker (2012a)].

can be relaxed in stages to achieve the end result of source localization and characterization. The assumptions for this work are:

1. Source in fixed position (location unknown)
2. Source applied at time $t = 300\,\mathrm{s}$ and removed at $t = 600\,\mathrm{s}$
3. Main heat flux $q'' = 0.930\,\mathrm{MW/m^2}$ over $0.00635\,\mathrm{m}$ diameter circular area while source applied (value obtained in previous study [Myers, Jorge, Walker, and Mutton (2010b,a); Myers, Jorge, Mutton, and Walker (in press, 2012)])
4. Secondary heating is characterized by a Gaussian with magnitude $q''_g = 100\,\mathrm{W/m^2}$ and spread $\sigma_g^2 = 0.0009\,\mathrm{m^2}$ while source applied
5. Convection coefficient $h = 3.20\,\mathrm{W/m^2K}$ on both sides of the plate (value obtained in previous study [Myers, Jorge, Walker, and Mutton (2010b,a); Myers, Jorge, Mutton, and Walker (in press, 2012)])
6. Convection coefficient $h = 3\,\mathrm{W/m^2K}$ on the plate edges

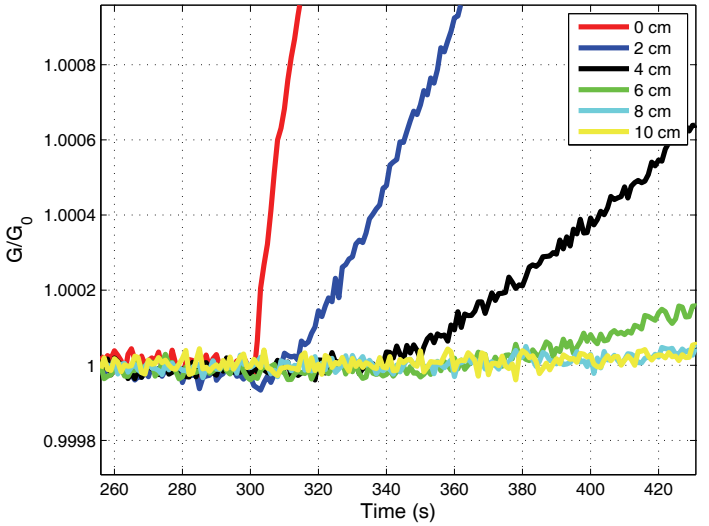

Figure 5: One-way ultrasonic pulse time of flight measurements for the beginning part of the heating phase [Myers, Jorge, Mutton, and Walker (2012a)].

7. Thermal conductivity $k = 14.6\,\mathrm{W/mK}$
8. Specific heat $C_p = 500\,\mathrm{J/kgK}$ and density $\rho = 8,000\,\mathrm{kg/m^3}$
9. Positions of sensors are ($\pm 4\,\mathrm{cm}$, $\pm 4\,\mathrm{cm}$) on the non-heated side
10. Measurement and filter updates are performed in real-time with 1 s time steps.

The 1 s time step is based on the need for continuous, real-time state estimation for an operational system. Selection of the time step for system implementation will depend upon resource requirements and performance. The heating source is located on the plate in the $x-y$ plane (x_q, y_q). The state therefore is $X_t = [x_q, y_q]^T$. The ultrasonic time of flight is normalized by the time of flight before the heating source is applied to the plate (G_{ij}/G_0).

The extended Kalman filter algorithm to locate the source can be found in Table 2. There is no input (U_t) to the state; thus the extended Kalman filter state model is $a = I_2$ and the state Jacobian is $A = I_2$, where I_2 is a 2×2 identity matrix. A state variance of $\sigma^2 = 0.0001\,\mathrm{m}^2$ was chosen as a baseline value. Thus, the state model

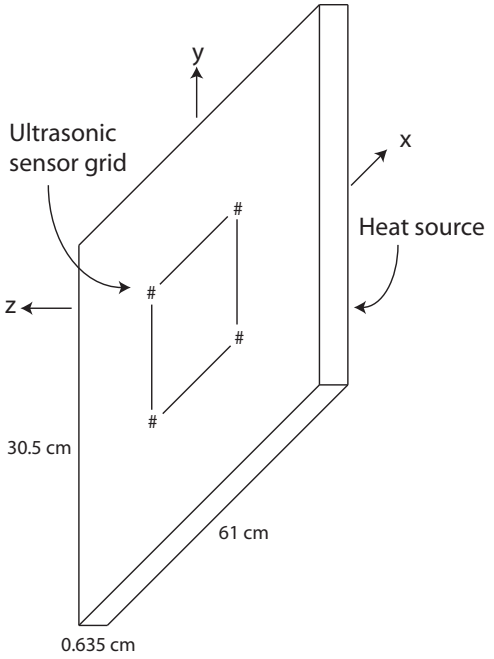

Figure 6: Ultrasonic sensor grid on the non-heated side of the plate with # symbols representing sensors and lines representing the ultrasonic pulse propagation paths between sensors (not drawn to scale) [Myers, Jorge, Mutton, and Walker (2012a)].

Table 2: Extended Kalman filter algorithm.

Step	Operation
1	$\overline{X}_t = a(U_t, X_{t-1})$
2	$\overline{\Sigma}_t = A_t \Sigma_{t-1} A_t^T + Q_t$
3	$K_t = \overline{\Sigma}_t B_t^T (B_t \overline{\Sigma}_t B_t^T + R_t)^{-1}$
4	$X_t = \overline{X}_t + K_t(Z_t - b(\overline{X}_t))$
5	$\Sigma_t = (I - K_t B_t)\overline{\Sigma}_t$
6	Return to Step 1 for next time step

covariance matrix is $Q_t = 0.0001\,\mathrm{m}^2 \times I_2$. Sensitivity to this parameter is discussed in the Section 6.

This measurement model consists of obtaining expected temperatures from COMSOL®,

computing the average temperature between the transducers, and then computing an expected time of flight to form $b(\overline{X}_t$ (equation 6). For the current analysis, the average temperature is computed along the path on the non-heated plate surface between the two sensors. The Jacobian partial derivatives are obtained using finite difference when moving the source in the x and y directions independently (equation 7).

$$b(\overline{X}_t) = \begin{bmatrix} \overline{G}_1 \\ \overline{G}_2 \\ \overline{G}_3 \\ \overline{G}_4 \end{bmatrix}; \tag{6}$$

$$B_t = \begin{bmatrix} -\frac{\partial \overline{G}_1}{\partial x_1} & -\frac{\partial \overline{G}_1}{\partial y_1} \\ -\frac{\partial \overline{G}_2}{\partial x_2} & -\frac{\partial \overline{G}_2}{\partial y_2} \\ -\frac{\partial \overline{G}_3}{\partial x_3} & -\frac{\partial \overline{G}_3}{\partial y_3} \\ -\frac{\partial \overline{G}_4}{\partial x_4} & -\frac{\partial \overline{G}_4}{\partial y_4} \end{bmatrix}, \tag{7}$$

where t is time in seconds with a time step of 1 s, $\overline{G}_i$ with $i = 1,2,3,4$ is the ultrasonic pulse time of flight with the heating source located at (x_s, y_s), and (x_i, y_i) with $i = 1,2,3,4$ are the locations of four transducers. The Jacobian B_t is constructed using the derivatives with respect to sensor position for convenience because this information can be obtained with one COMSOL® simulation. The derivatives are obtained from COMSOL® using finite differences by independently varying the x and y positions of all sensors by 0.0001 m. This value is based on a typical finite difference value of 0.1% multiplied by a unit length of 1 cm. Based on the flat plate experiment above, the sensor noise is assumed be $\pm 6 \times 10^{-4}$ (a non-dimensional number based on G_{ij}/G_0) and is normally distributed ($\sigma^2 = ((6 \times 10^{-4})/3)^2 = 4 \times 10^{-7}$). The measurement covariance matrix, therefore, is $R = 4 \times 10^{-7} \times I_4$. Extended Kalman filter convergence behavior with these parameters is illustrated in Figure 7 with the heating source located at ($x = 2$ cm, $y = 0$ cm) and an initial guess of ($x = 0$ cm, $y = 0$ cm). Examination of other heating source locations and initial guesses are explored in previous work [Myers, Jorge, Mutton, and Walker (2012a)].

6 Extended Kalman Filter Observations

Section 5 details the extended Kalman filter algorithm (Table 2) and the need for defining the state model covariance and the measurement covariance. This section details an examination of the extended Kalman filter as implemented for this heating source localization problem. The investigation encompasses sensitivity to changes in the state model covariance (Q), sensitivity to changes in the measure-

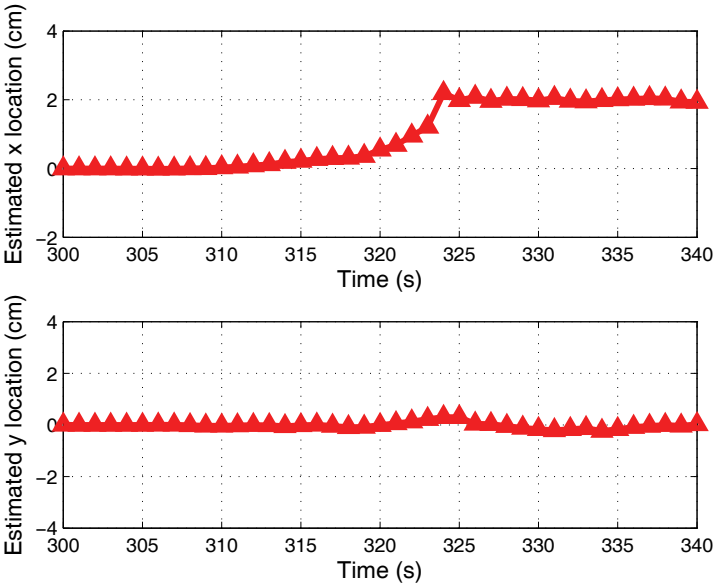

Figure 7: Extended Kalman filter convergence with the state model covariance values of $Q = 1 \times 10^{-4}\,\mathrm{m}^2 \times I_2$, measurement covariance values of $R = 4 \times 10^{-7} \times I_4$, heating source located at ($x = 2\,\mathrm{cm}$, $y = 0\,\mathrm{cm}$), and an initial guess of ($x = 0\,\mathrm{cm}$, $y = 0\,\mathrm{cm}$).

ment covariance (R), the possibility that Q and R are correlated, behavior during convergence of the state covariance matrix (Σ), and behavior during convergence of the Kalman gain (K_t). Sensitivities to the primary heat flux (q''), secondary heating magnitude and variance (q''_g and σ_g^2), convection coefficients (h_{sides} and h_{edges}), and thermal conductivity (k) are illustrated and analyzed in previous work Myers, Jorge, Mutton, and Walker (2012b). Additionally, this previous work details sensitivity to time of flight (G) measurement noise. This previous work concluded that the solution is fairly insensitive to noise and an inverse routine will be able to estimate heat flux (q'') and thermal conductivity (k) reliably, but the other parameters will have large confidence intervals and simultaneous estimation of these parameters will be difficult.

Figure 8 illustrates the sensitivity to the state model covariance by comparing values from $Q = 0.1\,\mathrm{m}^2 \times I_2$ to $0.000001\,\mathrm{m}^2 \times I_2$. Decreasing the state model covariance (Q) magnitude results in a damping effect on the convergence. Decreasing the magnitude too far causes the estimated position values to remain fairly constant

and the solution fails to converge. Conversely, increasing the state model covariance (Q) magnitude increases the convergence rate. Increasing the state model covariance (Q) too far results in erratic position estimates and the solution fails to converge.

Figure 9 illustrates the sensitivity to the measurement covariance by comparing values from $R = 4 \times 10^{-5} \times I_4$ to $R = 4 \times 10^{-10} \times I_4$. Increasing the measurement covariance (R) magnitude results in a damping effect on the convergence. Increasing the magnitude too far causes the estimated position values to remain fairly constant and the solution fails to converge. Conversely, decreasing the measurement covariance (R) magnitude increases the convergence rate. Decreasing the measurement covariance (R) too far results in erratic position estimates and the solution fails to converge.

A trend is evident when comparing Figures 8 and 9 in that Q and R appear to be inversely correlated. Figure 10 illustrates the relationship. Decreasing Q by one order of magnitude or increasing R by one order of magnitude results in similar convergence behavior. Likewise, increasing Q by one order of magnitude or decreasing R by one order of magnitude also results in similar convergence behavior. For example, using $Q = 0.0001\,\mathrm{m}^2 \times I_2$ and $R = 4 \times 10^{-7} \times I_4$ as the baseline, decreasing the state model covariance to $Q = 0.00001\,\mathrm{m}^2 \times I_2$ but keeping the measurement covariance at $R = 4 \times 10^{-7} \times I_4$ results in similar convergence behavior if the state model covariance is kept at $Q = 0.0001\,\mathrm{m}^2 \times I_2$ and the measurement covariance is increased to $R = 4 \times 10^{-6} \times I_4$.

We can conclude from these observations that the state model covariance (Q) and the measurement covariance (R) are correlated for this heating source localization scenario. The measurement covariance is determined from sensor noise, a measurable quantity, and the state model covariance is unknown and not measurable. Therefore, a large uncertainty exists in the state model covariance while a small uncertainty exists in the measurement covariance.

7 Adaptive Extended Kalman Filter

The goal of this work is to obtain faster and smoother convergence. Since the measurement covariance is known with a small uncertainty, the state model covariance is unknown, and the state model covariance and measurement covariance are correlated, an adaptive extended Kalman filter is envisioned where changes are made during each iteration to the state model covariance to improve convergence. A value is needed from the extended Kalman filter to drive changes to the state model covariance. Examining the extended Kalman filter (Table 2) reveals two possible sources: the Kalman gain (K_t) and the state covariance (Σ).

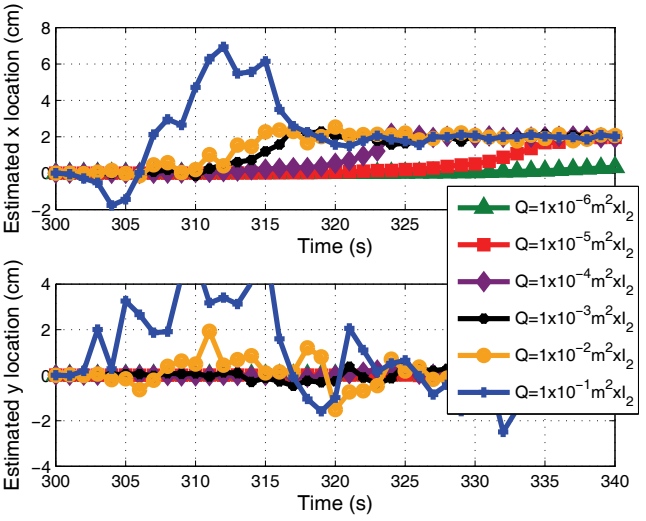

Figure 8: Extended Kalman filter convergence for a range of state model covariance values (Q) with constant measurement covariance values of $R = 4 \times 10^{-7} \times I_4$, the heating source located at ($x = 2\,\text{cm}$, $y = 0\,\text{cm}$), and an initial guess of ($x = 0\,\text{cm}$, $y = 0\,\text{cm}$).

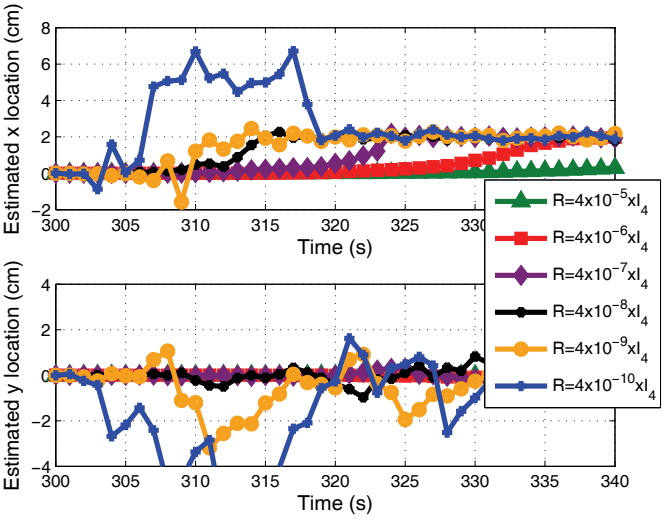

Figure 9: Extended Kalman filter convergence for a range of measurement covariance values (R) with constant state model covariance values of $Q = 1 \times 10^{-4}\,\text{m}^2 \times I_2$, the heating source located at ($x = 2\,\text{cm}$, $y = 0\,\text{cm}$), and an initial guess of ($x = 0\,\text{cm}$, $y = 0\,\text{cm}$).

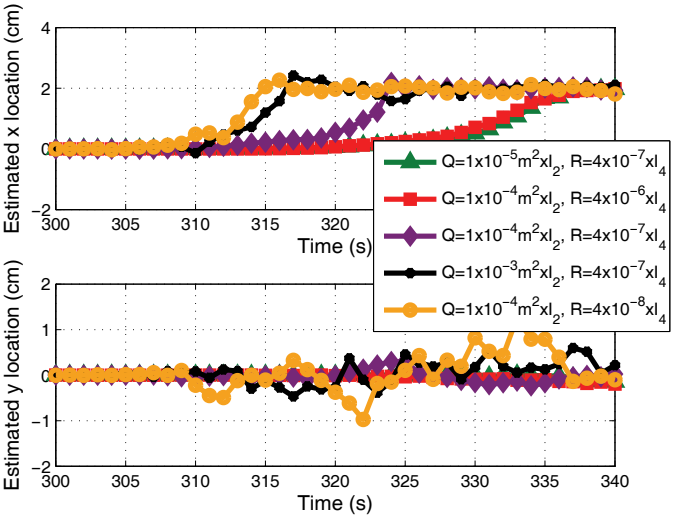

Figure 10: Extended Kalman filter convergence illustrating the correlation between the state model covariance matrix (Q) and the measurement covariance matrix (R). The heating source is located at ($x = 2\,\text{cm}$, $y = 0\,\text{cm}$) with an initial guess of ($x = 0\,\text{cm}$, $y = 0\,\text{cm}$).

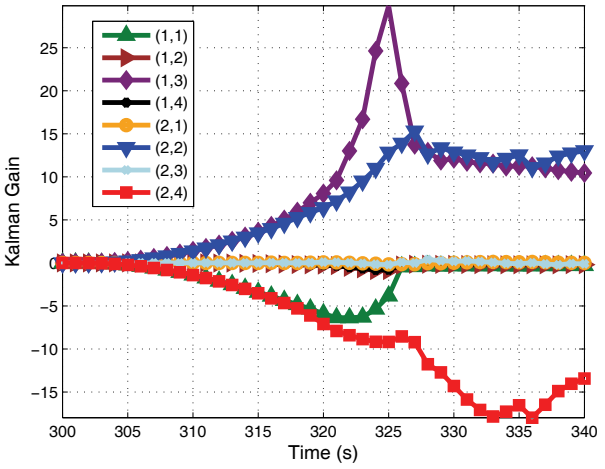

Figure 11: Kalman gain values during convergence for state model covariance of $Q = 1 \times 10^{-4}\,\text{m}^2 \times I_2$ and measurement covariance of $R = 4 \times 10^{-7} \times I_4$. The heating source is located at ($x = 2\,\text{cm}$, $y = 0\,\text{cm}$) with an initial guess of ($x = 0\,\text{cm}$, $y = 0\,\text{cm}$). Legend entries refer to the matrix element in the Kalman gain which is a 2×4 matrix. Convergence (from Figure 7) is at 324 s.

Figure 11 illustrates the magnitude of each element in the Kalman gain (K_t), which, for this heating source localization, is a 2×4 matrix. Comparing Figure 11 with Figure 7, the $(1,3)$ value from the Kalman gain (K_t) stands out as a possible source since it increases until convergence and then decreases rapidly. However, this value remains large even after convergence.

Figure 12 illustrates the normalized magnitude of the variance contained in the state covariance matrix (Σ) which is a 2×2 matrix in this heating source localization problem. The variance values are in the main diagonal of the matrix and are identical. Comparing with Figure 7, we observe that the variance increases steadily, decreases rapidly just before and during convergence, and remains small after convergence. Figure 13 illustrates the normalized magnitude of the variance for a range of state model covariance values from $Q = 1 \times 10^{-1}\,\mathrm{m}^2 \times I_2$ to $Q = 1 \times 10^{-6}\,\mathrm{m}^2 \times I_2$ and a measurement covariance of $R = 4 \times 10^{-7} \times I_4$. A comparison of Figure 13 with Figure 8 yields the observation that the variance increases steadily, decreases rapidly just before and during convergence, and remains small after convergence for every state model covariance examined.

Based on these observations, an adaptive extended Kalman filter is developed and is presented in Table 3. Step 6 is the only change from the extended Kalman filter found in Table 2. The state model covariance matrix Q is modified at the end of each iteration based on the state covariance Σ and the rate of change in the estimated state ΔX_t. Three conditions are possible when modifying Q. First, if the covariance is increasing at a rate greater than a predefined tolerance value and if the estimated state is changing less than a predefined limit, Q is multiplied by an predefined adaptive gain M. This adaptive gain will have a value greater than 1, which, in this first condition, has the effect of increasing the magnitude of Q and increasing the rate of convergence. From the analysis above, an increasing state covariance Σ indicates the solution is not converged and if the change in the estimate state is below a threshold, convergence time can be reduced by increasing the magnitude of Q. Second, if the covariance is increasing at a rate greater than a predefined tolerance value and if the estimated state is changing more than a predefined limit, Q is divided by the predefined gain M. In this second condition, increasing the magnitude of Q might cause erratic convergence or a failure to reach a solution. Thus, by reducing the magnitude of Q, convergence is dampened. Third, if the covariance is increasing at a rate less than a predefined tolerance value, no change is needed to Q.

8 Results

The adaptive extended Kalman filter developed above incorporates three new parameters. The predefined tolerance value $\Sigma_{tolerance}$ for changes to the state co-

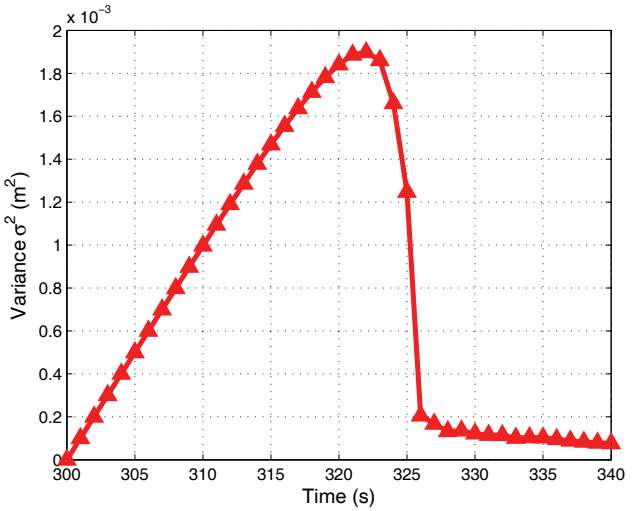

Figure 12: Variance (σ^2) from the state covariance matrix (Σ) for state model covariance of $Q = 1 \times 10^{-4}\,\mathrm{m}^2 \times I_2$ and measurement covariance of $R = 4 \times 10^{-7} \times I_4$. The heating source is located at $(x = 2\,\mathrm{cm},\ y = 0\,\mathrm{cm})$ with an initial guess of $(x = 0\,\mathrm{cm},\ y = 0\,\mathrm{cm})$. Convergence (from Figure 7) is at 324 s.

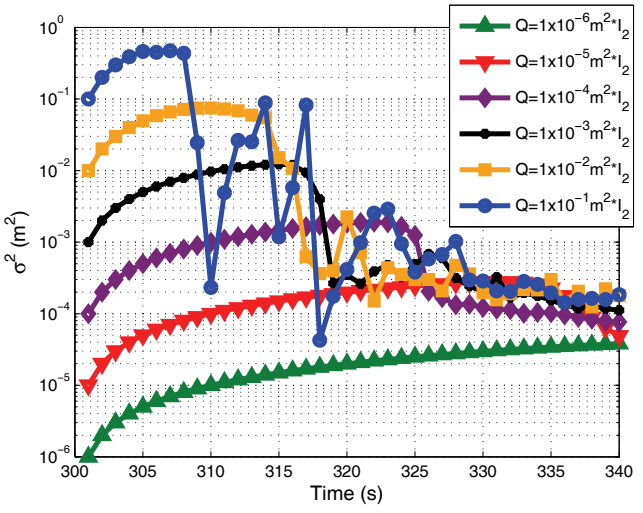

Figure 13: Variance (σ^2) from the state covariance matrix (Σ) for a range of state model covariance values (Q) and constant measurement covariance of $R = 4 \times 10^{-7} \times I_4$. The heating source is located at $(x = 2\,\mathrm{cm},\ y = 0\,\mathrm{cm})$ with an initial guess of $(x = 0\,\mathrm{cm},\ y = 0\,\mathrm{cm})$. Convergence behavior can be found in Figure 8.

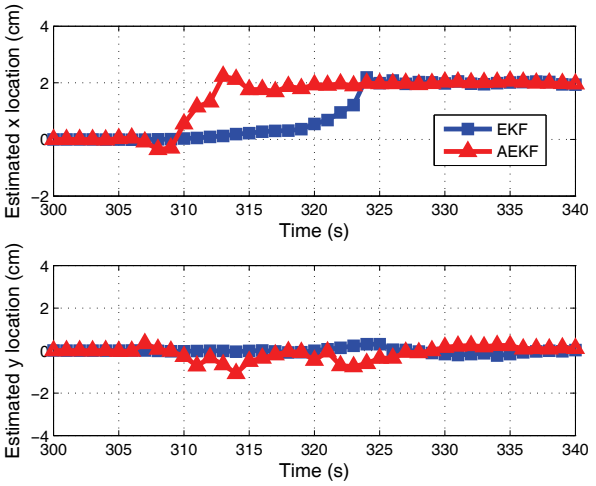

Figure 14: Extended Kalman filter and adaptive extended Kalman filter convergence with $Q_0 = 1 \times 10^{-4}\,\mathrm{m}^2 \times I_2$, $R = 4 \times 10^{-7} \times I_4$, and $M = 2$. The heating source is located at ($x = 2\,\mathrm{cm}$, $y = 0\,\mathrm{cm}$) with an initial guess of ($x = 0\,\mathrm{cm}$, $y = 0\,\mathrm{cm}$).

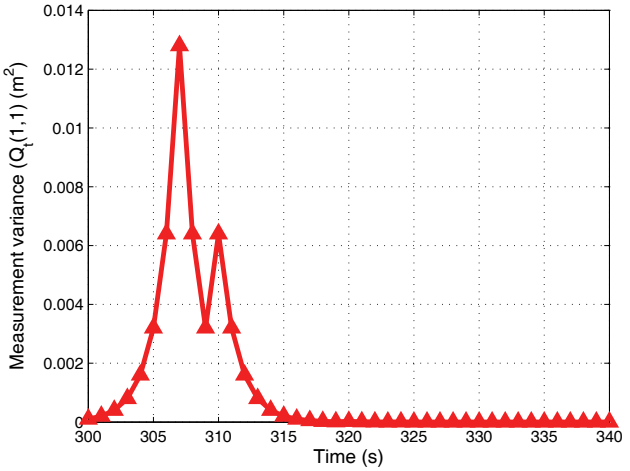

Figure 15: Adaptive extended Kalman measurement covariance (Q_t) values during convergence with $Q_0 = 1 \times 10^{-4}\,\mathrm{m}^2 \times I_2$, $R = 4 \times 10^{-7} \times I_4$, and $M_t = 2$. The heating source is located at ($x = 2\,\mathrm{cm}$, $y = 0\,\mathrm{cm}$) with an initial guess of ($x = 0\,\mathrm{cm}$, $y = 0\,\mathrm{cm}$).

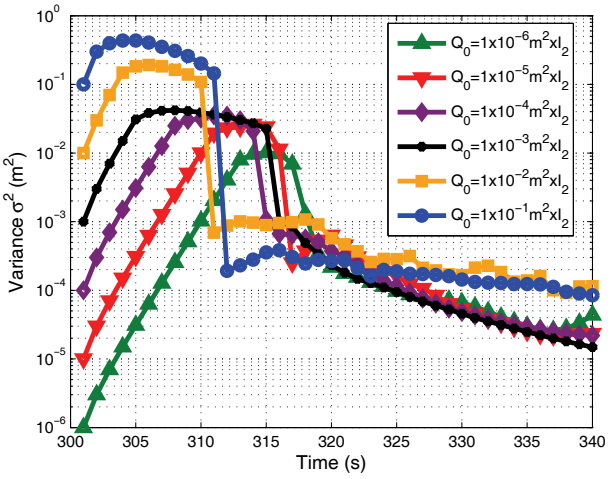

Figure 16: Adaptive extended Kalman filter variance (σ^2) from the state covariance matrix (Σ) for a range of starting state model covariance values (Q_0), constant measurement covariance of $R = 4 \times 10^{-7} \times I_4$, and $M_t = 2$. The heating source is located at ($x = 2\,\text{cm}$, $y = 0\,\text{cm}$) with an initial guess of ($x = 0\,\text{cm}$, $y = 0\,\text{cm}$).

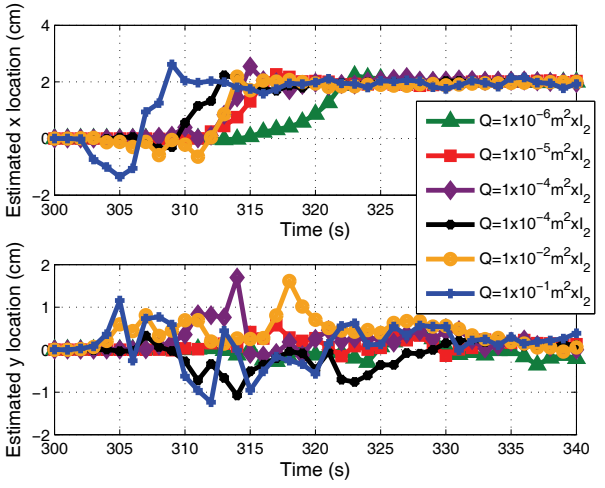

Figure 17: Adaptive extended Kalman filter convergence for a range of initial state model covariance values (Q_0), constant measurement covariance of $R = 4 \times 10^{-7} \times I_4$, and a state model covariance gain of $M = 2$. The heating source is located at ($x = 2\,\text{cm}$, $y = 0\,\text{cm}$) with an initial guess of ($x = 0\,\text{cm}$, $y = 0\,\text{cm}$).

Table 3: Adaptive extended Kalman filter algorithm.

Step	Operation
1	$\overline{X}_t = a(U_t, X_{t-1})$
2	$\overline{\Sigma}_t = A_t \Sigma_{t-1} A_t^T + Q_t$
3	$K_t = \overline{\Sigma}_t B_t^T (B_t \overline{\Sigma}_t B_t^T + R_t)^{-1}$
4	$X_t = \overline{X}_t + K_t (Z_t - b(\overline{X}_t))$
5	$\Sigma_t = (I - K_t B_t)\overline{\Sigma}_t$
6	$Q_{t+1} = \begin{cases} Q_t * M_t & \text{if } \lvert\Delta\Sigma_t\rvert > \Sigma_{tolerance} \text{ and } \Delta X_t < \Delta X_{limit} \\ Q_t / M_t & \text{if } \lvert\Delta\Sigma_t\rvert > \Sigma_{tolerance} \text{ and } \Delta X_t \geq \Delta X_{limit} \\ Q_t & \text{if } \lvert\Delta\Sigma_t\rvert \leq \Sigma_{tolerance} \end{cases}$
7	Return to Step 1 for next time step

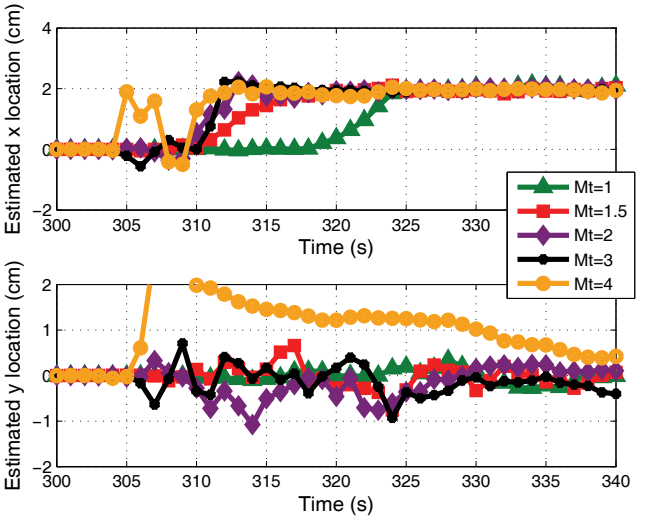

Figure 18: Adaptive extended Kalman filter convergence for a range of state model covariance gain values M, an initial state model covariance of $Q_0 = 1 \times 10^{-4}\,\mathrm{m}^2 \times I_2$, and constant measurement covariance of $R = 4 \times 10^{-7} \times I_4$. The heating source is located at ($x = 2\,\mathrm{cm}$, $y = 0\,\mathrm{cm}$) with an initial guess of ($x = 0\,\mathrm{cm}$, $y = 0\,\mathrm{cm}$).

variance Σ is based on the variance found in the first iteration and is defined as $\Sigma_{tolerance} = \Sigma_1$. The magnitude of Σ is dependent upon filter parameters including the state model covariance Q, thus basing the tolerance on the first iteration ensures the adaptive nature of the filter will smooth convergence near the converged solution. The predefined limit to convergence rate ΔX_{limit} for this work is defined as $\Delta X_{limit} = [\Delta x_{limit}, \Delta y_{limit}]^T = [1\,\text{cm/sec}, 1\,\text{cm/sec}]^T$. Figure 14 illustrates convergence for the adaptive extended Kalman filter with $Q_0 = 1 \times 10^{-4}\,\text{m}^2 \times I_2$, $R = 4 \times 10^{-7} \times I_4$, and an adaptive gain of $M_t = 2$. The adaptive extended Kalman filter outperforms the extended Kalman filter in this example. Figure 15 illustrates the variance value in Q during convergence for the adaptive extended Kalman filter. Q_t rises rapidly, peaks, falls rapidly, and then rises a second time before falling rapidly once again prior to convergence. Figure 16 illustrates the variance values from Σ for a range of initial state model covariance Q_0 values. Σ values drop significantly at the convergence time illustrated in Figure 17.

Figure 17 illustrates the effect that different initial state model covariance values has on the adaptive extended Kalman filter convergence. Comparing with Figure 8, the adaptive extended Kalman filter is able to converge quicker for a significant range of initial state model covariance values Q_0. Figure 18 illustrates the sensitivity to the adaptive extended Kalman filter gain M_t. Values for the gain from $M_t = 1.5$ to $M_t = 3$ produce similar results. Choosing a value for M_t outside of this range has detrimental effects on filter performance.

9 Conclusions

This work provides evidence that, for the heating source localization problem, the state model covariance and measurement covariance in the extended Kalman filter are correlated in an inversely proportional manner. Modifications to either the state model covariance or the measurement covariance effects the convergence behavior of the Kalman filter. The variance (diagonal elements in the state covariance matrix Σ), during convergence, was observed to increase until convergence and decrease rapidly after convergence. The variance was used to drive modifications to the state model covariance in a manner designed to affect convergence behavior. The adaptive extended Kalman filter developed in this work produces faster and smoother convergence than the non-adaptive form of the extended Kalman filter. This performance boost is accomplished by tailoring the state model covariance during each iteration instead of retaining the assumed state model covariance throughout the convergence process. Kalman filter successes in robotics and other fields lies in its simplicity, computational efficiency, and the existence of a control input. Whereas this work had no inputs to the state model, the ability to add inputs to the extended Kalman filter is anticipated to be robust for heating source localization.

Acknowledgement: The authors would like to acknowledge the financial support from the United States Air Force Research Laboratory (AFRL) under contract FA8650-08-C-3829 and the Brazilian agency Conselho Nacional de Desenvolvimento Científico e Tecnológico (CNPq). The authors would also like to acknowledge Dr. Mitch Wilkes, Associate Professor of Electrical Engineering and Associate Professor of Computer Engineering at Vanderbilt University for his assistance in understanding recursive state estimation.

References

Beck, J.; Woodbury, K. (1998): Inverse problems and parameter estimation: integration of measurements and analysis. *Measurement Science and Technology*, vol. 9, pp. 839–847.

Berger, K.; Rufer, S.; Kimmel, R.; Adamczak, D. (2009): Aerothermodynamic characteristics of boundary layer transition and trip effectiveness of the HIFiRE flight 5 vehicle. In *AIAA Proceedings*, no. AIAA-2009-4055.

Bertin, J.; Cummings, R. (2003): Fifty years of hypersonics: where we've been, where we're going. *Progress in Aerospace Sciences*, vol. 39, no. 6-7, pp. 511–536.

Bertsekas, D. P. (1996): Incremental least squares methods and the extended Kalman filter. *SIAM Journal on Optimization*, vol. 6, no. 3, pp. 807–822.

Corigliano, A.; Mariani, S. (2004): Parameter identification in explicit structural dynamics: performance of the extended Kalman filter. *Computer Methods in Applied Mechanics and Engineering*, vol. 193, no. 36-38, pp. 3807–3835.

Corigliano, A.; Mariani, S.; Orsatti, B. (2000): Identification of Gurson-Tvergaard material model parameters via Kalman filtering technique. I. Theory. *International Journal of Fracture*, vol. 104, no. 4, pp. 349–373.

Dowding, K. J.; Blackwell, B. F. (2001): Sensitivity analysis for nonlinear heat conduction. *Journal of Heat Transfer*, vol. 123, no. 1, pp. 1.

Fay, J.; Riddell, F. (1958): Theory of stagnation point heat transfer in dissociated air. *Journal of the Aeronautical Sciences*, vol. 25, no. 2, pp. 73–85.

Gai, S.; Hayne, M. (2010): Heat transfer behind a step in high-enthalpy laminar hypersonic flow. *Journal of Thermophysics and Heat Transfer*, vol. 24, no. 4, pp. 839–841.

Gan, C.; Danai, K. (2001): Nonlinear state estimation by adaptive embedded RBF modules. *Journal of Dynamic Systems, Measurement, and Control*, vol. 123, no. 1, pp. 44–48.

Ghanem, R.; Spanos, P. (1990): Polynomial chaos in stochastic finite elements. *Journal of Applied Mechanics*, vol. 57, no. 1, pp. 197–202.

Heffes, H. (1966): The effect of erroneous models on the Kalman filter response. *IEEE Transactions on Automatic Control*, vol. 11, no. 3, pp. 541–543.

Horvath, T. J.; Berry, S. A.; Hollis, B. R. (2002): Boundary layer transition on slender cones in conventional and low disturbance Mach 6 wind tunnels. In *32nd AIAA Fluid Dynamics Conference and Exhibit*, no. AIAA-2002-2743, St. Louis, MO. AIAA.

Kamiński, M. (2005): On generalized stochastic perturbation-based finite element method. *Communications in Numerical Methods in Engineering*, vol. 22, no. 1, pp. 23–31.

Kendall, J. (1975): Wind tunnel experiments relating to supersonic and hypersonic boundary-layer transition. *AIAA Journal*, vol. 13, no. 3, pp. 290–299.

Kozlov, V.; Adamchik, V.; Lipovtsev, V. (1989): Local heating of an unbounded orthotropic plate through a circular and annular domain. *Journal of Engineering Physics and Thermophysics*, vol. 57, pp. 1381–1391.

Maier, G.; Bocciarelli, M.; Bolzon, G.; Fedele, R. (2006): Inverse Analyses in Fracture Mechanics. *International Journal of Fracture*, vol. 138, no. 1-4, pp. 47–73.

Majji, M.; Juang, J.-N.; Junkins, J. L. (2010): Observer/Kalman-filter time-varying system identification. *Journal of Guidance, Control, and Dynamics*, vol. 33, no. 3, pp. 887–900.

Malik, M. (1989): Prediction and control of transition in supersonic and hypersonic boundary layers. *AIAA Journal*, vol. 27, no. 11, pp. 1487–1493.

Mehra, R. (1969): On the identification of variances and adaptive Kalman filtering (adaptive Kalman filtering with unknown process and measurement noise covariance matrices). *IEEE Transactions on Automatic Control*, vol. 15, pp. 175–184.

Myers, M. R.; Jorge, A. B.; Mutton, M. J.; Walker, D. G. (2012): A comparison of extended Kalman filter, particle filter, and least squares localization methods for a high heat flux concentrated source. *International Journal of Heat and Mass Transfer*, vol. 55, no. 9-10, pp. 2219–2228.

Myers, M. R.; Jorge, A. B.; Mutton, M. J.; Walker, D. G. (2012): High heat flux point source sensitivity and localization analysis for an ultrasonic sensor array. *International Journal of Heat and Mass Transfer*, vol. 55, no. 9-10, pp. 2472–2485.

Myers, M. R.; Jorge, A. B.; Mutton, M. J.; Walker, D. G. (in press, 2012): A comparison of extended Kalman filter ultrasound time-of-flight measurement models for heating source localisation. *Inverse Problems in Science and Engineering*. (in press).

Myers, M. R.; Jorge, A. B.; Walker, D. G.; Mutton, M. J. (2010): A comparison of extended Kalman filter approaches using non-linear temperature and ultrasound time-of-flight measurement models for heating source localization of a transient heat transfer problem. In *Inverse Problems, Design and Optimization Symposium*, no. IPDO-027, Brazil. IPDO.

Myers, M. R.; Jorge, A. B.; Walker, D. G.; Mutton, M. J. (2010): A comparison of extended Kalman filter, extended information filter, and least squares approaches for parameter identification of a transient heat transfer problem. In *Inverse Problems Symposium*, East Lansing, MI. Michigan State University.

Myers, M. R.; Walker, D. G.; Yuhas, D. E.; Mutton, M. J. (2008): Heat flux determination from ultrasonic pulse measurements. In *International Mechanical Engineering Congress and Exposition*, no. IMECE2008-69054. ASME.

Myers, M. R.; Walker, D. G.; Yuhas, D. E.; Mutton, M. J. (in review, 2010): Heat flux determination from ultrasonic pulse measurements. *International Journal of Heat and Mass Transfer*. (in review).

Park, H.; Jung, W. (2001): On the solution of multidimensional inverse heat conduction problems using an efficient sequential method. *Journal of Heat Transfer*, vol. 123, no. 6, pp. 1021–1029.

Raudenský, M.; Woodbury, K. A.; Kral, J.; Brezina, T. (1995): Genetic algorithm in solution of inverse heat conduction problems. *Numerical Heat Transfer, Part B: Fundamentals*, vol. 28, no. 3, pp. 293–306.

Reed, H. L.; Kimmel, R. L.; Schneider, S.; Arnal, D.; Saric, W. (1997): Drag prediction and transition in hypersonic flow. In *Symposium on Sustained Hypersonic Flight, AGARD Conference on Future Aerospace Technology in the Service of the Alliance*, Palaiseau, France. NATO Research and Technology Organisation.

Roache, P. J. (1998): *Verification and Validation in Computational Science and Engineering*. Hermosa Publishers.

Rochinha, F. A.; Peirce, A. (2010): Monitoring hydraulic fractures: state estimation using an extended Kalman filter. *Inverse Problems*, vol. 26, pp. 1–18.

Schneider, S. (1999): Flight data for boundary-layer transition at hypersonic and supersonic speeds. *Journal of Spacecraft and Rockets*, vol. 36, no. 1, pp. 8–20.

Schneider, S. (2004): Hypersonic laminar-turbulent transition on circular cones and scramjet forebodies. *Progress in Aerospace Sciences*, vol. 40, no. 1-2, pp. 1–50.

Schook, R.; Lange, H. D.; Steenhoven, A. V. (2001): Heat transfer measurements in transitional boundary layers. *International Journal of Heat and Mass Transfer*, vol. 44, no. 5, pp. 1019–1030.

Thrun, S.; Burgard, W.; Fox, D. (2006): *Probabilistic Robotics*. The MIT Press.

Tuan, P.; Ju, M. (2000): The validation of the robust input estimation approach to two-dimensional inverse heat conduction problems. *Numerical Heat Transfer, Part B: Fundamentals*, vol. 37, no. 2, pp. 247–265.

Vianna, F.; Orlande, H.; Dulikravich, G. (2009): Prediction of the temperature field in pipelines with Bayesian filters and non-intrusive measurements. In *Proceedings of the 20th International Congress of Mechanical Engineering*, Gramado, RS, Brazil.

Wang, H.; Chen, T.; Tuan, P.; Den, S. (2005): Adaptive-weighting input-estimation approach to nonlinear inverse heat-conduction problems. *Journal of Thermophysics and Heat Transfer*, vol. 19, no. 2, pp. 209–216.

Xu, C.; Gertner, G. (2008): Uncertainty and sensitivity analysis for models with correlated parameters. *Reliability Engineering & System Safety*, vol. 93, no. 10, pp. 1563–1573.

Yang, J. N.; Lin, S.; Huang, H.; Zhou, L. (2006): An adaptive extended Kalman filter for structural damage identification. *Structural Control and Health Monitoring*, vol. 13, no. 4, pp. 849–867.

Yucelen, T.; Calise, A. J. (2010): Kalman filter modification in adaptive control. *Journal of Guidance, Control, and Dynamics*, vol. 33, no. 2.

Zhou, L.; Wu, S.; Yang, J. (2008): Experimental study of an adaptive extended Kalman filter for structural damage identification. *Journal of Infrastructure Systems*.

CMES: Computer Modeling in Engineering & Sciences

ISSN : 1526-1492 (Print); 1526-1506 (Online)

Journal website:
http://www.techscience.com/cmes/

Manuscript submission
http://submission.techscience.com

Published by
Tech Science Press
5805 State Bridge Rd, Suite G108
Duluth, GA 30097-8220, USA

Phone (+1) 678-392-3292
Fax (+1) 678-922-2259
Email: sale@techscience.com
Website: http://www.techscience.com
Subscription: http://order.techscience.com

CMES is Indexed & Abstracted in
Applied Mechanics Reviews; Cambridge Scientific Abstracts (Aerospace and High Technology; Materials Sciences & Engineering; and Computer & Information Systems Abstracts Database); CompuMath Citation Index; Current Contents: Engineering, Computing & Technology; Engineering Index (Compendex); INSPEC Databases; Mathematical Reviews; MathSci Net; Mechanics; Science Alert; Science Citation Index; Science Navigator; Zentralblatt fur Mathematik.